

Article

# Devising Strain Hardening Models Using Kocks–Mecking Plots—A Comparison of Model Development for Titanium Aluminides and Case Hardening Steel

Markus Bambach <sup>1,\*</sup>, Irina Sizova <sup>1</sup>, Sebastian Bolz <sup>2</sup> and Sabine Weiß <sup>2</sup>

<sup>1</sup> Chair of Mechanical Design and Manufacturing, Brandenburg University of Technology Cottbus-Senftenberg, Konrad-Wachsmann-Allee 17, Cottbus D-03046, Germany; sizova@b-tu.de

<sup>2</sup> Chair of Physical Metallurgy and Materials Technology, Brandenburg University of Technology Cottbus-Senftenberg, Konrad-Wachsmann-Allee 17, Cottbus D-03046, Germany; sebastian.bolz@b-tu.de (S.B.); sabine.weiss@b-tu.de (S.W.)

\* Correspondence: bambach@b-tu.de; Tel.: +49-355-69-3108

Academic Editor: Hugo F. Lopez

Received: 29 June 2016; Accepted: 22 August 2016; Published: 29 August 2016

**Abstract:** The present study focuses on the development of strain hardening models taking into account the peculiarities of titanium aluminides. In comparison to steels, whose behavior has been studied extensively in the past, titanium aluminides possess a much larger initial work hardening rate, a sharp peak stress and pronounced softening. The work hardening behavior of a TNB-V4 (Ti–44.5Al–6.25Nb–0.8Mo–0.1B) alloy is studied using isothermal hot compression tests conducted on a Gleeble 3500 simulator, and compared to the typical case hardening steel 25MoCrS4. The behavior is analyzed with the help of the Kocks–Mecking plots. In contrast to steel the TNB-V4 alloy shows a non-linear course of  $\theta$  (i.e., no stage-III hardening) initially and exhibits neither a plateau (stage IV hardening) nor an inflection point at all deformation conditions. The present paper describes the development and application of a methodology for the design of strain hardening models for the TNB-V4 alloy and the 25CrMoS4 steel by taking the course of the Kocks–Mecking plots into account. Both models use different approaches for the hardening and softening mechanisms and accurately predict the flow stress over a wide range of deformation conditions. The methodology may hence assist in further developments of more sophisticated physically-based strain hardening models for TiAl-alloys.

**Keywords:** titanium aluminides alloy; single phase steel; hot forming; dynamic recrystallization; modeling

## 1. Introduction

Intermetallic titanium aluminides (TiAl) alloys are relatively new class of lightweight materials which can be applied in automotive applications as well as in aviation gas turbines where they have to withstand temperatures up to 800 °C. The high potential of TiAl for these applications stems from the fact that the TiAl-based alloys have remarkable mechanical properties, such as a low specific weight of about 4 g/cm<sup>3</sup>, a high strength at elevated temperatures and a very good oxidation/corrosion resistance [1–3]. In recent years, forgeable  $\beta$ -solidifying TiAl alloys have been developed with the goal of exploiting the benefits of the hot-worked microstructure, which allows for better performance than the as-cast state. However, as many other intermetallic alloys titanium aluminides are brittle, even at elevated temperatures.

An important task in processing TiAl to products consists in overcoming problems associated with the limited workability of TiAl-based alloys and the robust design of forging processes. With the rapid

development of computing techniques, Finite Element (FE) simulation is widely applied nowadays to study metal forming processes. In metal forming, the accuracy of FE simulations depends crucially on the constitutive model. It is hence very important to establish a precise constitutive model for the flow stress which predicts the dependence of flow stress on deformation temperature, strain rate, and strain. In the past, various analytical, phenomenological [4–6] and empirical models [7–9] have been devised to model the strain hardening behavior of ordinary single phase steels. For steels, hardening is usually modeled using semi-empirical material models. For softening caused by dynamic recrystallization, the Johnson-Avrami-Mehl-Kolmogorov (JMAK) equation is commonly used.

The existing models have been successfully applied to steel and also transferred to TiAl. Extensive studies have been carried out to describe the flow stress as a function of temperature, strain rate and strain of the TiAl-alloys. Cheng et al. [10] adopt the model proposed by Laasraoui and Jonas [11] to TiAl-alloys with a nominal composition of Ti–42Al–8Nb–0.2W–0.1Y (at %). Godor et al. [12] applied two phenomenological constitutive models, the Sellars–McTegart model [13] and the Hensel–Spittel model [14], for the description of the deformation behavior of two  $\gamma$ -TiAl alloys with nominal compositions Ti–41Al–3Mo–0.5Si–0.1B and Ti–45Al–3Mo–0.5Si–0.1B. He et al. [15] and Pu et al. [16] established a constitutive model based on Arrhenius-type equations and the sine hyperbolic description for the Zener–Hollomon parameter for a Ti–45Al–8.5Nb–(W,B,Y) alloy and for a TiAl–Cr–V alloy, respectively. Deng et al. [17] proposed a flow stress model of Ti–47Al-alloy based on a regression analysis using Hensel–Spittel model. All existing descriptions of the flow behavior of TiAl-alloys are based on empirical models, which were derived primarily for steels. Steels are typically hot-worked in the austenitic phase, i.e., the models are designed for microstructure evolution in a single phase material.

In contrast to steel, TiAl-alloys have a complex multi-phase microstructure during hot working. The understanding of the flow behavior of TiAl alloys under hot deformation conditions thus has a great importance for the design of hot working processes. The majority of studies show that the flow curves of TiAl-based intermetallic alloys exhibited a sharp peak stress at a relatively low strain. Then, the flow stress decreased rapidly into a steady-state stress. Previous research [18–21] reported that dynamic recrystallization contributes to flow softening. Several other influencing factors have been reported, involving most notably flow localization that is partly initiated by dynamic recrystallization and adiabatic heating during deformation [21]. Hot compression tests with various TiAl-alloys with different primary structures have shown that the primary structure strongly influences the material behavior during hot forming [22]. Semiatin et al. [23,24] and Schaden et al. [25] concluded that the presence of lamellar colonies is responsible for a strong softening during hot forming (i.e., the pronounced maximum in the course of the flow curves).

It is known that the strain hardening rate  $\theta = \partial\sigma/\partial\varepsilon$  as a function of flow stress (this type of plot is often referred to as Kocks–Mecking plot) reveals different stages of microstructure evolution during hot deformation as characteristic stages [26]. Ordinary single phase alloys such as steels in the austenitic phase exhibit at first a linearly decreasing strain hardening rate (stage III hardening) followed by a slowly decreasing hardening rate called stage IV, before attaining stage V where the values of  $\theta$  approach zero [4,27]. Steels, which are hot-compression-tested in the austenitic phase, show inflection points in Kocks–Mecking plots that correspond to the onset of DRX [28]. In contrast to the ones of steel, the Kocks–Mecking plots of TiAl-alloys initially decrease monotonically, but not with a linear rate. Recent research of the authors has shown that TiAl-alloys initially show a non-linear, concave down course of  $\theta$  (i.e., no stage-III hardening) and exhibit neither a plateau (stage IV hardening) nor an inflection point under all tested conditions [29].

The aim of this study is to investigate the peculiarities of the work hardening behavior of a Ti–44.5Al–6.25Nb–0.8Mo–0.1B (in at %) TiAl-alloy by direct comparison to a typical 25MoCrS4 steel used for forging by means of isothermal hot compression tests. It is shown how the features of the TiAl-alloy affect the set-up of strain hardening models. Special attention is paid on the accuracy of the strain hardening model in  $\theta$ – $\sigma$ -space, which is typically not taken into account in model development.

The paper is structured as follows: Section 2 gives an overview of the TNB-V4 alloy and 25MoCrS4 steel and the performed hot compression tests. Section 3 details the flow curves, Kocks-Mecking plots and metallographic results. The methodology for designing strain hardening models based on the behavior observed in the Kocks-Mecking plots is presented in Section 4, which also details the parameter identification procedure. In Sections 5 and 6, a comparison of the model results to experimental data and final conclusions are presented.

## 2. Materials and Hot Compression Testing

We studied a high Nb containing TiAl alloy with a nominal composition of Ti–44.5Al–6.25Nb–0.8Mo–0.1B (in at %) and a 25MoCrS4 steel with the chemical composition of 0.25 wt % C, 0.25% Si, 0.70% Mn, 1.05% Cr, 0.25% Mo, balance Fe. In order to start with chemically homogeneous samples the TiAl alloy was prepared by VAR melting. Residual porosity was removed by hot isostatic pressing at 1260 °C for 4 h with a pressure of 200 bars. A Gleeble 3500 thermo-mechanical simulator (DSI Europe GmbH, Weissenhorn, Germany) was used to simulate the hot forging process by means of hot compression tests. Strain measurement was performed with the standard LVDT (Linear variable differential transformer) of the Gleeble machine (DSI Europe GmbH, Weissenhorn, Germany). The testing temperatures ranged from 1150 °C to 1300 °C and the strain rates ranged from 0.001 s<sup>-1</sup> to 0.5 s<sup>-1</sup>. Compression tests were conducted in vacuum of 10<sup>-4</sup> mbar. The specimens were heated with a heating rate of 10 K/s and held for 5 min to obtain a homogeneous microstructure before compression testing.

In order to investigate the microstructure evolution under hot working conditions, each specimen was quenched immediately after upsetting. Metallographic examination was carried out on cross sections parallel to the compression direction of the deformed specimens. The sections were also analyzed using scanning electron microscopy (Tescan Orsay Holding, Brno-Kohoutovice, Česká Republika).

The 25MoCrS4 steel was analyzed by compression testing in previous work of the first author of this paper [30]. Cylindrical specimens with a diameter of 10 mm and a height of 15 mm were deformed at temperatures ranging from 700 °C to 1200 °C, and strain rates from 0.01 s<sup>-1</sup> to 100 s<sup>-1</sup>. In all tests, the specimens were first heated from room temperature to 1250 °C and homogenized for 10 min, then placed into the furnace of the compression testing machine (Servotest Testing Systems Ltd., Surrey, UK) and cooled to the specific deformation temperature. The maximum true strain obtained in all tests was ~0.8. All specimens were quenched after testing and examined for grain size and recrystallized volume fractions.

## 3. Experimental Results

### 3.1. Hot Deformation Behavior

Figure 1 illustrates the true stress–strain curves at deformation temperature of 1200 °C and different strain rates in the isothermal compression of the 25MoCrS4 steel (Figure 1a) and the TNB-V4-alloy (Figure 1b). It can be seen that the hot deformation behavior of the TNB alloy is in strong contrast to the behavior of the 25MoCrS4 steel, which is fully austenitic under the testing conditions.

It is observed that the isothermal compression behavior of the 25MoCrS4 steel is approximately divided into three stages: (i) The flow stress increases to a peak value ( $\sigma_p$ ) with increasing strain; (ii) The flow stress decreases to a steady state value. In this stage the softening becomes increasingly predominant due to the onset of DRX; (iii) The flow stress keeps a steady state due to the dynamic balance between work hardening and softening induced by DRX. It is apparent that the flow curves of steel display the typical characteristic of softening by DRX. Typical Kocks-Mecking plots ( $\theta$ – $\sigma$  curves) of the 25MoCrS4 steel at 1200 °C and various strain rates are shown in Figure 1c. The steel exhibits a characteristic work-hardening behavior. At first,  $\theta$  decreases linearly (so called stage-III hardening) until reaching an inflection point, which determines the critical stress ( $\sigma_c$ ) and accordingly the onset

of DRX [28]. Just before the inflection point, the working hardening rate decreases to a lower slope (stage IV hardening). After the onset of DRX,  $\theta$  decreases rapidly towards the peak stress ( $\sigma_p$ ), at which  $\dot{\theta} = 0$ . The  $\theta$ – $\sigma$  curves can be used to determine the onset of DRX.

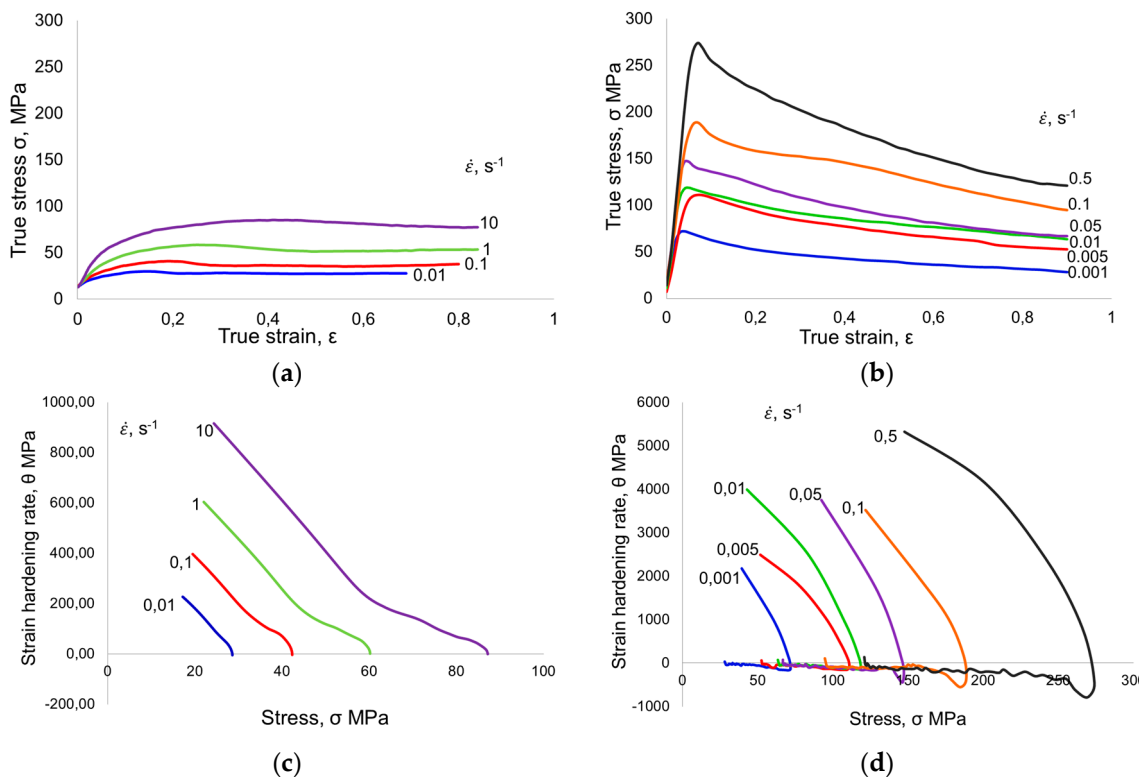


**Figure 1.** The flow stress curves at temperature 1200 °C and various strain rates: (a) for single phase steel 25MoCrS4; (b) for TNB-V4-alloy; (c) Kocks-Mecking plots of 25MoCrS4; and (d) Kocks-Mecking plots of TNB-V4-alloy.

In contrast to the flow curves of the 25MoCrS4 steel, the TNB-V4 alloy has a high initial hardening with a pronounced flow stress maximum, which is much sharper than for steel in the austenitic range. Then, the flow stress decreases rapidly to a steady-state stress with increasing strain, albeit with a different curvature than steel. The measured flow curves of TNB-V4 show a very strong dependence on strain rate and temperature. The flow stress increases very rapidly with increasing strain rate and decreasing temperature. In contrast to steel, it can be seen (Figure 1d) that the Kocks-Mecking plots of TNB-V4 look absolutely different. The alloy under investigation neither shows a linear initial decrease of  $\dot{\theta}$  (i.e., no stage-III hardening) nor does it exhibit a plateau (stage IV hardening) or an inflection point at all forming conditions. The work-hardening behavior of the TNB-V4-alloy can be explained by the complex multiphase microstructure, and many factors that may affect the hot deformation behavior of TiAl-alloys, such as flow localization, additional interior adiabatic heating, rotation or buckling and breakdown of the lamellar colonies during hot forming, cf. [31].

It has to be mentioned here that measurement accuracy, adiabatic heating, inhomogeneous deformation as well as further processing of the recorded data will affect the computation of stress-strain curves and the derivatives of the stress strain curves, which form the basis of the Kocks-Mecking plots used in this paper. In previous work by Lohmar and Bambach [32], the processing of recorded data was treated in detail with respect to the computation of Kocks-Mecking plots. The effect and correction of adiabatic heating was treated in Xiong et al. [33]. Data processing in the present paper was performed according to these findings. The stress-strain curves and Kocks-Mecking plots should hence well represent the behavior of the material.

### 3.2. Microstructure Evolution

The microstructure of the latest industrially used generation of Titanium aluminides consists of globular  $\gamma$ -grains,  $\alpha + \gamma$ -lamellar colonies and an increased amount of  $\beta/\beta_0$ -grains along the boundaries of lamellar colonies. Compared with two phase alloys, the stabilization of the  $\beta/\beta_0$ -phase leads to a better strength-ductility ratio. Especially the workability of these TiAl-alloys is better than the one of previous generations of TiAl-alloys [34]. The deformation in two-phase  $\alpha_2 + \gamma$ -alloys is mainly based on dislocation glide and twinning in the  $\gamma$ -phase combined with deformation anisotropy of the lamellar colonies. The anisotropy of the lamellar colonies leads to soft or hard deformation modes depending on the direction of the applied stress. The yield and fracture stresses are low if the deformation occurs parallel to the lamella plane. In the opposite case the stresses are high if the deformation occurs perpendicular to the lamellae [35]. Under load hard mode, colonies rotate into flow direction or a kinking of the lamellas occurs. As can be seen in Figure 2b, after kinking both parts of the colonies subsequently rotate into flow direction during forming. It can be assumed that, depending on the bcc structure of the  $\beta$ -phase and its ordered counterpart  $\beta_0$ , both phases have a sufficient amount of independent slip modes. That leads, combined with the limited deformability of the  $\alpha$ - and  $\gamma$ -phase, to a high deformation gradient between the different phases. As a consequence, the  $\beta/\beta_0$ -phase acts as a lubricant for the whole microstructure and supports the rotation of hard mode lamellar  $\alpha_2 + \gamma$ -colonies [36]. It is hence assumed that the rotation of the  $\alpha_2 + \gamma$ -colonies from hard into soft orientations leads to a non-linear course of strain hardening rate in the Kocks-Mecking plots.

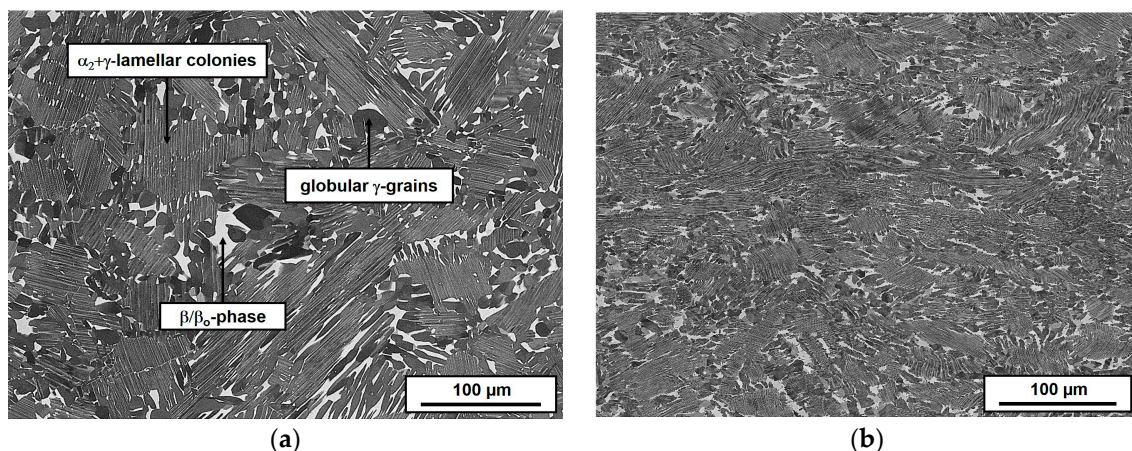


**Figure 2.** Typical microstructures of TNB-V4: (a) as-cast + HIP (hot isostatic pressing) state and (b) compressed at 1250 °C with a strain rate of 0.25 s<sup>-1</sup> to a strain of 60%.

## 4. Microstructure-Based Strain Hardening Models for Hot Working

### 4.1. Derivation of Model Equations

Various microstructure-based strain hardening models have been derived in the past (see, e.g., Bariani et al. [37] for a review). For steel, dynamic recrystallization (DRX) is a dominant softening mechanism which restores the deformed microstructure during forming and allows for large plastic deformations without failure of the workpiece. Most strain hardening models rely on Johnson-Mehl-Avrami-Kolmogorov (JMAK) kinetics for DRX. Poliak and Jonas [28] showed that the onset of DRX corresponds to an inflection point in the course of the strain hardening rate  $\theta$  as a function of stress  $\sigma$ , i.e., the critical stress is a root of the second derivative of the strain hardening rate with respect to stress:

$$\frac{\partial}{\partial \sigma} \left( -\frac{\partial \theta}{\partial \sigma} \right) = 0 \quad (1)$$

Recently, two problems in modeling the strain hardening behavior under hot working conditions were discovered: (i) inconsistency of JMAK kinetics with the Poliak-Jonas criterion; and (ii) absence of an inflection point in practical experiments despite occurrence of DRX [38].

Since the criterion by Poliak and Jonas was derived from principles of irreversible thermodynamics and has been confirmed with experimental data, a flow stress model that takes DRX into account should adhere to this criterion, not only to be consistent with experimental data but also to make sure that the model is sound in a thermodynamical sense. Hence, the flow stress  $\sigma$  should be three times continuously differentiable with respect to  $\varepsilon$ . It was recently shown by Bambach [38] that the Poliak-Jonas criterion requires that the Avrami exponent exceeds a value of 3 for the model to be consistent with the criterion. Hence, generalized transformation kinetics was considered to find the root cause of the inconsistency and to alleviate them. As mentioned in the introduction, TiAl alloys do not seem to show an inflection point in  $\theta$  in spite of the occurrence of DRX [29].

A flow stress model that includes DRX essentially consists of four types of equations: (i) a model for strain hardening and dynamic recovery of the non-recrystallized material; (ii) an initiation criterion for DRX; (iii) DRX kinetics and an equation for the recrystallized grain size; and (iv) a rule of mixture to determine the macroscopic flow stress when recrystallized and non-recrystallized grains coexist. In addition, the evolution of grain size is expressed by an additional equation, which is mostly not coupled to the flow stress model.

Various model choices for the individual parts of the model are available. Due to the large differences in strain hardening behavior for different materials, setting up a model for a certain material requires to take the peculiarities of the strain hardening and softening of the material into account. As a consequence, there does not seem to be a unified model that would be applicable to all kinds of materials. In the following, we describe the features of typical strain hardening models that take DRX into account. We then show how to devise and select the model equations so that a suitable model is attained, at the example of the case hardening steel and the TNB alloy.

**Model equations for characteristic points.** Semi-empirical material models are the most commonly used models in industrial applications. They are often preferred to physically-based models due to their fast computing times. The basic idea behind semi-empirical models is that characteristic points of the flow curves can be expressed as a function of the Zener-Hollomon parameter  $Z$ . A typical semi-empirical model based on the equations proposed by Luton and Sellars [39] and Beynon and Sellars [40] is given in Figure 3 together with an illustration of a flow curve, the strain hardening rate and their characteristic points.

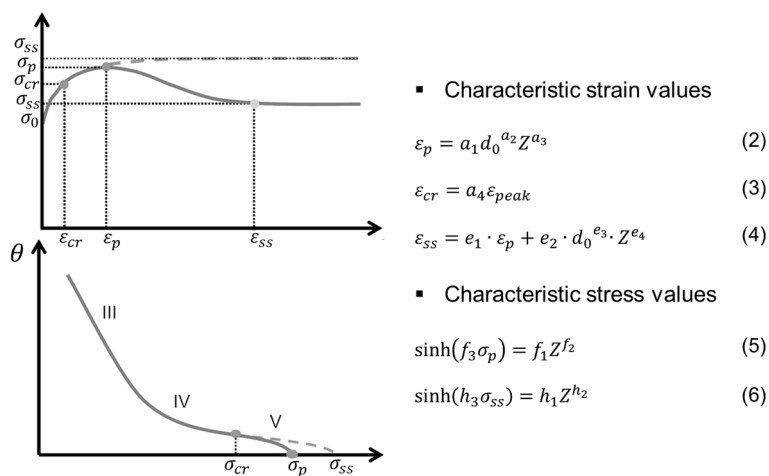


**Figure 3.** Flow curve and strain hardening rate with characteristic point and model equations for the Beynon and Sellars model [40].

The strain at which the maximum value of the flow stress is attained is given by Equation (2). The critical strain for the initiation of DRX is assumed to be a constant fraction  $a_4$  of  $\varepsilon_p$  by Equation (3). The strain at which a steady state deformation is reached is given by Equation (4), which uses four fit parameters,  $e_1$ – $e_4$ . The peak and steady state flow stress  $\sigma_p$  and  $\sigma_{ss}$  are modeled as functions of the Zener-Hollomon parameter  $Z$  via Equations (5) and (6), with material-dependent parameters  $f_1, f_2, f_3$  and  $h_1, h_2, h_3$ .

**Strain hardening.** A plenitude of models is available to model strain hardening. Recent research has shown that different kinds of inconsistencies with the Poliak-Jonas criterion can occur depending on the model choice [38]. If the strain hardening models do not show an inflection point, they do not reach the critical point. If the strain hardening model shows an inflection point, care must be taken that the inflection point coincides with the critical conditions of DRX nucleation models. In addition, the model might just not capture the course of the strain hardening rate in a Kocks-Mecking plot in the right way, which shows that the underlying physics are not taken into account.

Typical dislocation density models are formulated as ordinary differential equations, which contain terms for the generation and annihilation of dislocations. These models were derived from physical mechanisms of dislocation theory. The Taylor equation correlates dislocation density to the macroscopic flow stress. It can be used to transform the model equations into  $\theta$ - $\sigma$ -space (Kocks-Mecking plots), where the course of the strain hardening rate can be analyzed. None of the dislocation-based models detailed in Table 1 are appropriate for the TNB alloy since they cannot reproduce the curvature in a Kocks-Mecking plot. The phenomenological model by Cingara and McQueen, however, possesses the right curvature for  $C \geq 1$ . The constant  $C$  determines the curvature of the flow curve up to the peak. The location of the peak is explicitly taken into account by the strain hardening model. Softening will be superimposed after the onset of DRX and will be discussed below.

In contrast, the model by Cingara and McQueen is not the best choice for the 25MoCrS4 steel. The 25MoCrS4 steel shows all hardening stages, i.e., a linear decrease of  $\theta(\sigma)$  initially, which is referred to as stage-III hardening, an stage IV hardening with a reduced softening rate and an inflection point, and a subsequently increased softening rate due to DRX.

In physical theories of crystal plasticity, the dislocation density is commonly used as the structural parameter for macroscopic descriptions of plastic flow, with the flow stress governed by Taylor-like hardening following:

$$\sigma = \sigma_0 + \alpha G b \sqrt{\rho} \quad (7)$$

where  $\sigma_0$  is the yield stress, at which point  $\rho = \rho_0$  and  $\varepsilon = \varepsilon_0$ ,  $\alpha$  is a constant of 0.5–1,  $G$  is the shear modulus, and  $b$  is the Burger's vector. The Taylor equation can be utilized to transform the model equations into Kocks-Mecking plots. Equally, models can be formulated directly in the  $\theta$ - $\sigma$ -space and then transferred into stress-strain curves based on the Taylor equation. The strain hardening model proposed in [38] reproduces the course of the experimentally observed  $\theta$ - $\sigma$ -curves using a linear function for the initial stage-III hardening, a transition to a second linear function which represents stage IV and then, starting from the critical point, a cubic function of stress is used to model stage V hardening. Hence, the model is designed to mimic the hardening behavior observed for steel (cf. Figure 1c), but it would not be applicable to TNB-V4.

**Recrystallization kinetics.** In the original work of Luton and Sellars [39], JMAK kinetics was proposed for DRX, which were formulated as function of time. Later, a strain-dependent version of the kinetics was introduced by Sellars [41]. Recent research has shown that JMAK kinetics is only consistent with the Poliak-Jonas criterion if the Avrami exponent exceeds a value of 3 [38]. As a consequence, DRX kinetics based transformation kinetics that go back on Cahn were proposed, which are detailed in Table 2. In contrast, the softening of TNB is not only determined by DRX but also by the rotation and break-down of lamellar colonies, adiabatic heating etc. Since consistency to the Poliak-Jonas criterion is not an issue for TNB-V4 (it shows no inflection point), ordinary JMAK kinetics may be used, albeit with no physical meaning.

**Table 1.** Comparison of different strain hardening models and their course in Kocks-Mecking plots  $\theta(\sigma)$ .

Evolution of $\rho$	Flow Stress	$\theta(\sigma)$	Curvature	Form/Reference
$\frac{d\rho}{d\varepsilon} = k_1\sqrt{\rho} - k_2\rho$	$\sigma(\varepsilon) = \sigma_0 + (\sigma_{ss} - \sigma_0)(1 - e^{-C\varepsilon})$	$\theta(\sigma) = C(\sigma_{ss} - \sigma)$	None (linear course)	 [4]
$\frac{d\rho}{dt} = \frac{\dot{\varepsilon}}{bl} - 2M\tau\rho^2$ $\rho = \rho_s\tanh(2M\tau\rho_s\varepsilon/\dot{\varepsilon})$	$\sigma(\varepsilon) = \sigma_0 + \alpha G b \sqrt{\rho}$	$\theta(\sigma) = \frac{\alpha^2 G^2 b}{2l(\sigma - \sigma_0)} - \frac{M\tau(\sigma - \sigma_0)^3}{\alpha^2 G^2 b^2 \dot{\varepsilon}}$	Concave up/concave down	 [42] [43]
$\frac{d\rho}{d\varepsilon} = k_1 - k_2\rho$	$\sigma = \left[ \sigma_{ss}^{*2} + (\sigma_0^2 - \sigma_{ss}^{*2})e^{-\Omega\varepsilon} \right]^{1/2}$	$\theta(\sigma) = \frac{\Omega}{2} \left( \frac{\sigma_{ss}^2}{\sigma} - \sigma \right)$	Concave up	 [11]
-	$\sigma(\varepsilon) = \sigma_p \left[ \frac{\varepsilon}{\varepsilon_p} \exp(1 - \frac{\varepsilon}{\varepsilon_p}) \right]^C$	N.A.	concave down for $C \geq 1$	 [44]
-	N.A.	$\theta(\sigma) = \theta_{III}(1 - H_1(\sigma - \sigma_{IV})) + \theta_{IV}H_1(\sigma - \sigma_{IV}) + \theta_VH_2(\sigma - \sigma_V)$ $\theta_{IV} = b_{IV} - m_{IV}\sigma$ $\theta_V = -C(\sigma - \sigma_c)^3$ $H_1(x) = \frac{1}{2} + \frac{1}{2}\tanh(cx) = \frac{1}{1+e^{-2cx}}$	linear (stage III)/linear (stage IV)/concave down	 [38]

**Table 2.** Model equations for 25MoCrS4 and TNB.

Model Part	25MoCrS4 Steel	TNB
Strain hardening	$\theta(\sigma) = \theta_{\text{III}}(1 - H_1(\sigma - \sigma_{\text{IV}})) + \theta_{\text{IV}}H_1(\sigma - \sigma_{\text{IV}}) + \theta_{\text{V}}H_2(\sigma - \sigma_{\text{V}})$ $\theta_{\text{IV}} = b_{\text{IV}} - m_{\text{IV}}\sigma$ $\theta_{\text{V}} = -C(\sigma - \sigma_c)^3$ $H_{1,2}(x) = \frac{1}{2} + \frac{1}{2}\tanh(c_{(1,2)}x) = \frac{1}{1+e^{-2c_{(1,2)}x}}$	$\sigma(\varepsilon) = \sigma_p \left[ \frac{\varepsilon}{\varepsilon_p} \exp(1 - \frac{\varepsilon}{\varepsilon_p}) \right]^C$
Critical strain	$\varepsilon_{cr} = \alpha \varepsilon_p$ (Equation (3), s. Figure 3)	
Peak strain	$\varepsilon_p = a_1 \cdot d_0^{a_2} \cdot Z^{a_3}$ (Equation (2), s. Figure 3)	
Steady state stress	$\varepsilon_{ss} = e_1 \cdot \varepsilon_m + e_2 \cdot d_0^{e_3} \cdot Z^{e_4}$ (Equation (4), s. Figure 3)	
Peak stress	$\sinh(f_3 \cdot \sigma_p) = f_1 \cdot Z^{f_2}$ (Equation (5), s. Figure 3)	
Steady state stress	$\sinh(h_3 \cdot \sigma_p) = h_1 \cdot Z^{h_2}$ (Equation (6), s. Figure 3)	
DRX kinetics	$\dot{X}(t) = (1 - X(t)) \left[ \begin{array}{l} (1 - H(t_{ss}, t_s)) \frac{4\pi}{3} I_s S v^3 t^3 \\ + H(t_{ss}, t_s) A X(t) \end{array} \right]$	$X = 1 - \exp \left[ k \cdot \left( \frac{\varepsilon - \varepsilon_{cr}}{\varepsilon_{ss} - \varepsilon_{cr}} \right)^q \right], \quad \varepsilon \geq \varepsilon_{cr}$
Flow stress	$\sigma_Y = \begin{cases} \sigma_0 & \text{if } \varepsilon < \varepsilon_{cr} \\ \sum_{i=0}^{n-1} (X_i - X_{i+1}) \sigma_i + X_n \sigma_n & \text{if } \varepsilon \geq \varepsilon_{cr} \end{cases}$	

**Dynamically recrystallized grain size.** The dynamically recrystallized grain size is independent of the initial grain size and only depends on the Zener-Hollomon parameter via

$$d_{\text{DRX}} = b_1 \cdot Z^{b_2} \quad (8)$$

This equation is used in almost all semi-empirical models for DRX. In this work, it is applied to the 25MoCrS4 steel and to the phases of the TNB alloy that show recrystallization.

**Strain hardening models.** Based on the observations made about the strain hardening behavior of TNB-V4 and 25MoCrS4, two strain hardening models have been set up, which are detailed in Table 2. Both models are designed to meet the requirements of the materials

Using non-linear regression by least-squares, the models have been fitted to a single flow curve of TNB-V4 and 25MoCrS4, respectively. Figure 4 shows that for a single flow curve, the models reproduce not only the flow curves but also the behavior in the Kocks-Mecking plot with very high accuracy. When the model is applied to a larger range of temperatures and strain rates, parameter identification by non-linear regression may fail. To allow for successful parameter fitting, most of the model equations are first fitted to the experimental data using the characteristic points extracted from the flow curves. Regression is thus performed separately for each model equation. In the model, all equations are coupled. Hence, a non-linear regression of the entire model is performed subsequently, which will improve the initial parameter values obtained by fitting the model equations individually. The procedure is described in detail in the subsequent sections.

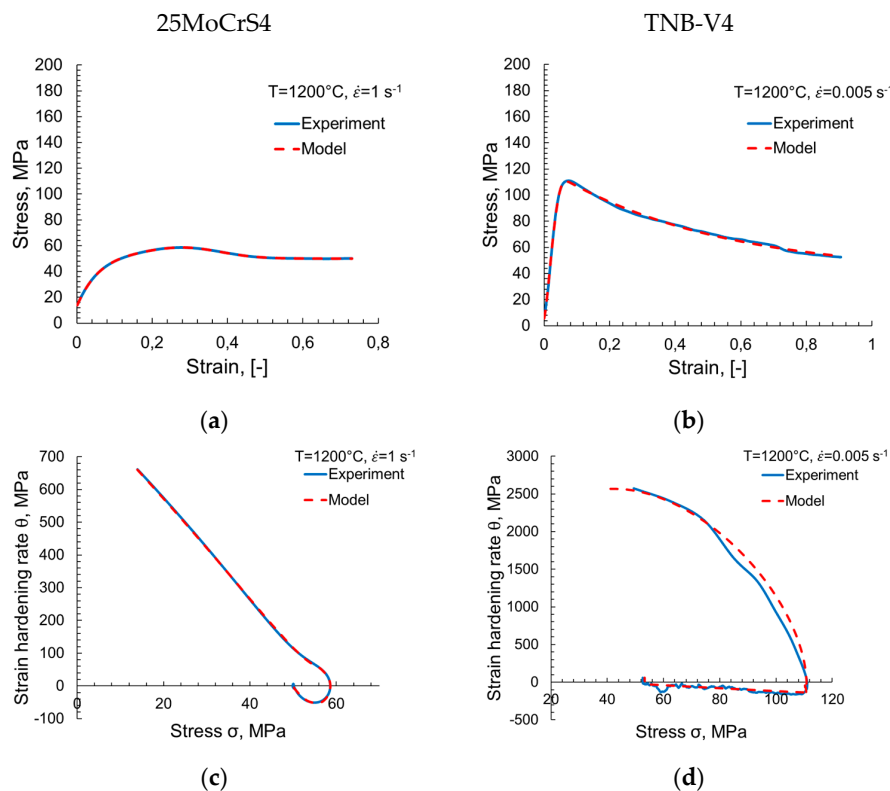


**Figure 4.** Model prediction vs. experimental data: (a) flow curve of 25MoCrS4; (b) flow curve of TNB-V4; (c) Kocks-Mecking plot of 25MoCrS4; and (d) Kocks-Mecking plot of TNB-V4.

#### 4.2. Evaluation of Experimental Data and Parameters Identification

The procedures for parameter identification depend largely on the model equations. However, some steps are common for the two models defined in Table 2 above. As a first step, all characteristic points such as  $\varepsilon_p$ ,  $\sigma_p$ ,  $\varepsilon_{ss}$ , and  $\sigma_{ss}$  have to be determined from the experimental flow curves.

Using  $\sigma_p$ , the activation energy and hence the Zener-Hollomon parameter  $Z$ , sometimes referred to as temperature-compensated strain rate, can be determined,

$$Z = \dot{\varepsilon} \exp\left(\frac{Q_w}{RT}\right) = A [\sinh(\alpha\sigma)]^n \quad (9)$$

where  $A$  and  $\alpha$  are constants,  $T$  is the deformation temperature,  $\sigma$  is the flow stress (MPa),  $\dot{\varepsilon}$  is the strain rate ( $s^{-1}$ ),  $n$  is the stress exponent,  $R$  is the gas constant ( $kJ \cdot mol^{-1} \cdot K^{-1}$ ) and  $Q_w$  is the activation energy of deformation ( $kJ \cdot mol^{-1}$ ).

For some model parameters (predominantly those with a physical background), dedicated procedures exist for parameter determination. The activation energy of hot working  $Q_w$ , for instance, can be determined from the following relation:

$$Q_w = R \left\{ \frac{\partial \ln \dot{\varepsilon}}{\partial \ln [\sinh(\alpha\sigma)]} \right\}_T \left\{ \frac{\partial \ln [\sinh(\alpha\sigma)]}{\partial (1/T)} \right\}_{\dot{\varepsilon}} \quad (10)$$

According to Poliak and Jonas [28], the critical strain  $\varepsilon_{cr}$  for the onset of DRX can be detected from the inflection point in the course of the strain hardening rate  $\theta = \partial\sigma/\partial\varepsilon$  as a function of flow stress  $\sigma$ . To this end, the strain hardening rate has to be computed from flow stress data. All other model parameters of the equations in Figure 3 can be determined for each equation independently by regression analysis.

A specific problem with the TNB alloy is that it shows no inflection point in the Kocks-Mecking plot. Hence, no critical stress or strain can be determined from flow stress data only.

To describe the relation between the dynamically recrystallized volume fraction  $X$  and strain an Avrami-type equation is used for TNB-V4 while different kinetics are used for 25MoCrS4 to ensure consistency with the Poliak-Jonas criterion. The model parameters are not determined from the flow curves but from the recrystallized fractions determined by quantitative metallography of quenched specimens. Based on the phase fraction and grain size of the different phases in the not deformed state a histogram for every phase was calculated. These histograms were used as basis to determine the differences of the phase fractions and grain sizes after deformation.

In the same way, the coefficients  $b_1$  and  $b_2$  in Equation (8), which describes the dynamically recrystallized grain size, were identified from metallographic evaluation of the specimens that show DRX.

#### 4.3. Determination of Model Parameters Common to Both Models

In this section, the experimental data from the cylinder compression tests and the metallographic analysis are used to determine the parameters for the strain hardening models. For this purpose, firstly the characteristic points such as  $\varepsilon_p$ ,  $\sigma_p$ ,  $\varepsilon_{ss}$ , and  $\sigma_{ss}$  were determined from the flow curves shown in Figure 1.

Based on Equation (10), the slope of the plots of  $\ln[\sinh(\alpha\sigma)]$  versus  $\ln\dot{\varepsilon}$  and  $1/T$  can be utilized for calculating the value of  $Q_w$ . The required plots are shown in Figure 5. Values of  $481.3 \text{ kJ} \cdot \text{mol}^{-1}$  for 25MoCrS4 and  $321.2 \text{ kJ} \cdot \text{mol}^{-1}$  for TNB-V4 were obtained for the activation energy  $Q_w$ .

In Figure 6a, a plot of the peak strain as a function of the Zener-Hollomon parameter is shown together with the results of regression analysis. The steady state strain strongly influences the shape of the flow curves. The extraction of values for the steady state strain is complicated for TNB-V4 since only a few flow curves attain a steady state regime. To determine the parameters  $e_1$ ,  $e_2$ , and  $e_3$  in Equation (4), which defines the dependence of  $\varepsilon_{ss}$  on the Zener-Hollomon parameter, a regression analysis was performed as shown in Figure 6b.

Since the TNB-V4-alloy shows no inflection point in the Kocks-Mecking plots no critical stress/strain can be determined from flow stress data only and  $\alpha$  was set to 0.5 from experience. For 25MoCrS4 previous work showed that a value of  $0.7\varepsilon_p$  is suitable.

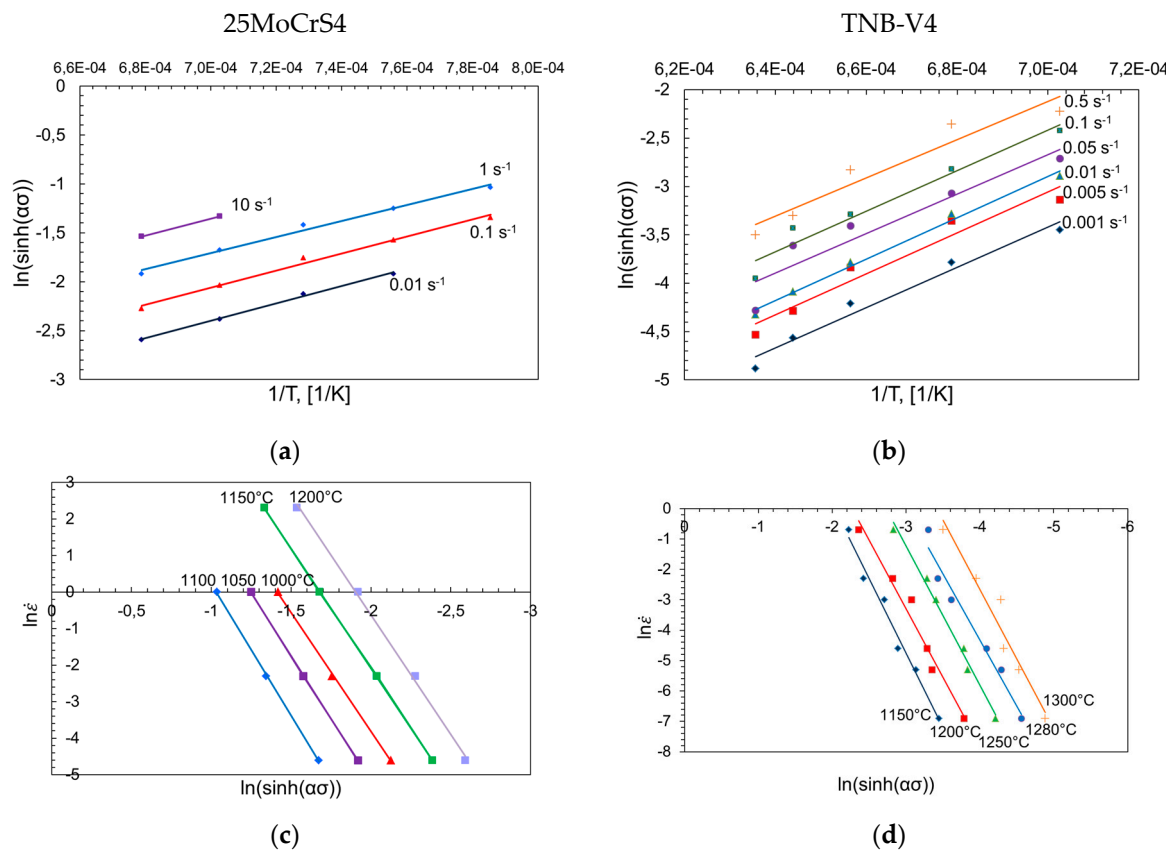


**Figure 5.** Evaluating  $Q_w$ :  $\ln[\sinh(\alpha\sigma)]$  versus  $1/T$  (a) for 25MoCrS4 and (b) for TNB-V4; and  $\ln\dot{\epsilon}$  versus  $\ln[\sinh(\alpha\sigma)]$  (c) for 25MoCrS4 and (d) for TNB-V4.

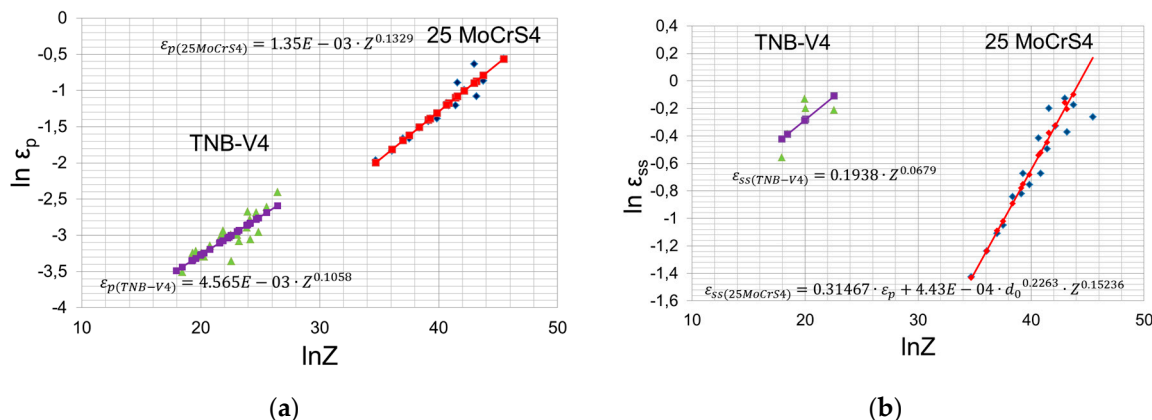


**Figure 6.** Strain depending on Zener-Hollomon-Parameter: (a) relationships between  $\ln\dot{\epsilon}_p$  and  $\ln Z$ ; and (b) relationships between  $\ln\dot{\epsilon}_{ss}$  and  $\ln Z$ .

The dependence of peak and steady state stress on the Zener-Hollomon parameter was determined by non-linear regression using Equations (5) and (6). The fitted and measured values are shown in Figure 7. As mentioned above, the equation of Cingara et al. [44] was employed to describe the work-hardening condition of TNB-V4-alloy up to the peak stress. Hence, the fitted peak stress values can be used directly.

The dynamically recrystallized grain size of 25MoCrS4 increases with decreasing Zener-Hollomon parameter, i.e., by increase of temperature and decrease of strain rate the resulting grain size increases.

In Figure 8a, the grain sizes determined for various  $Z$  values are shown along with the best fit of Equation (8). The kinetics of dynamic recrystallization is displayed in Figure 8b.

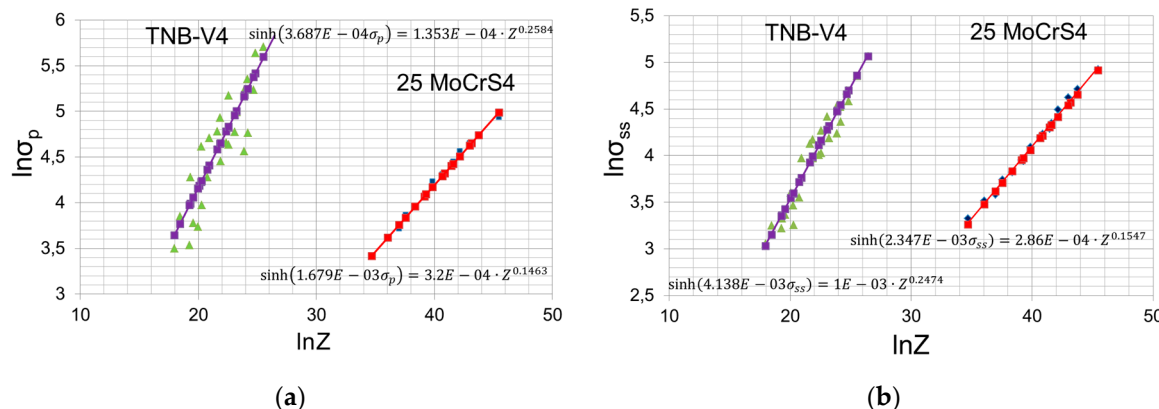


**Figure 7.** Stress depending on Zener-Hollomon-Parameter: (a) relationships between  $\ln \sigma_p$  and  $\ln Z$ ; and (b) relationships between  $\ln \sigma_{ss}$  and  $\ln Z$ .

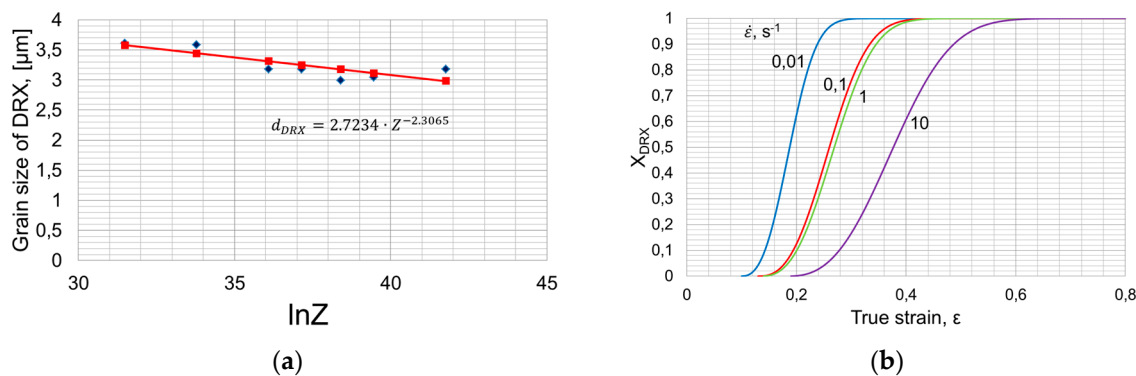


**Figure 8.** (a) Relationship between DRX grain size and Zener-Hollomon-Parameter; and (b) volume fraction of DRX obtained at a temperature of 1200 °C and different strain rates.

The relationship between the dynamically recrystallized grain size of the TNB-V4-alloy and the Zener-Hollomon-Parameter is shown in Figure 9. In the multiphase TiAl-alloys, solely the  $\beta/\beta_0$ - (Figure 9a) and  $\gamma$ -phase (Figure 9b) show recrystallization. The  $\alpha$ -phase only forms during hot forming. The typical microstructure of the TNB-V4-alloy after forming can be seen in Figure 9c.

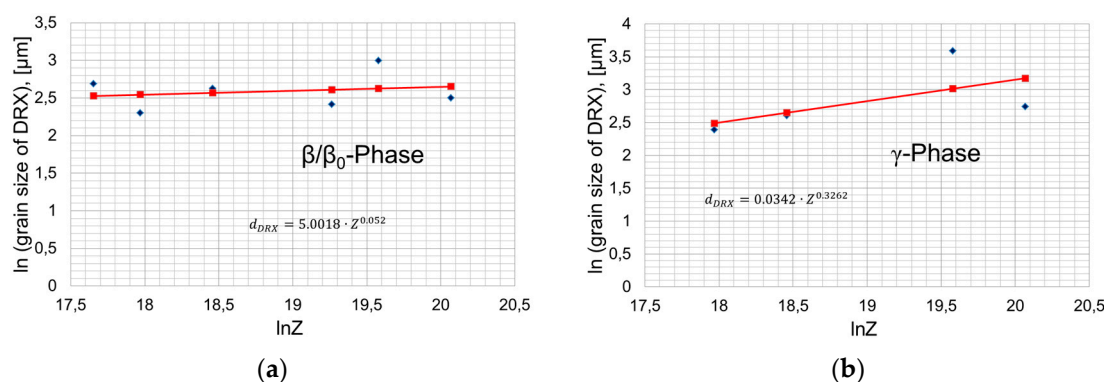


**Figure 9. Cont.**

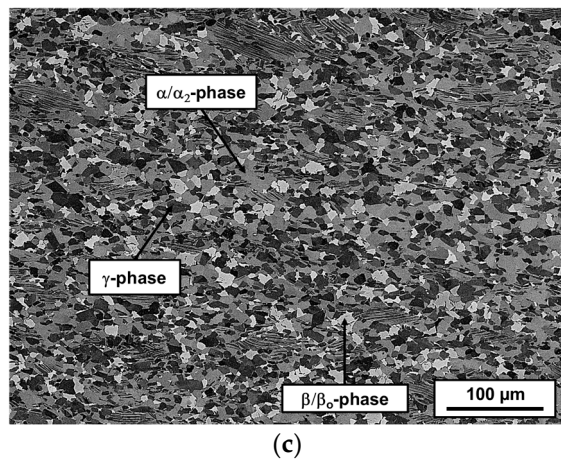


**Figure 9.** Relationship between DRX grain size and Zener-Hollomon-Parameter of TNB-V4: (a) for  $\beta/\beta_0$ -Phase; and (b)  $\gamma$ -Phase. (c) Typical microstructure of TNB-V4 compressed at 1250 °C with a strain rate of 0.001  $s^{-1}$  to a strain of 60%.

## 5. Final Calibration and Validation of the Model

The direct determination of model parameters detailed in section 4 is not applicable to all model parameters. In addition, since the interplay of the individual parts of the model determines the accuracy of the model, an inverse parameter identification is favorable as final step, i.e., after starting values of most model parameters are available from the direct determination performed in Section 4. Inverse parameter identification is essentially the solution of an optimization problem. The cost function is the sum of squares of the differences between measured and calculated flow stress values for all available values from the experiments:

$$F(\beta) = \sum_i \sum_j \sum_k (\sigma_f^{(exp)}(T_i, \dot{\epsilon}_j, \epsilon_k) - \sigma_f^{(sim)}(T_i, \dot{\epsilon}_j, \epsilon_k, \beta))^2 \quad (11)$$

The cost function  $F(\beta)$  is minimized using an optimization algorithm such as the Levenberg-Marquardt method to determine the material parameters, which are assembled in the parameter vector  $\beta$ .

Figure 10 shows a comparison between the predicted and measured flow stress values for the 25MoCrS4 steel for temperatures ranging from 900 °C to 1200 °C and five different strain rates. The model parameters were determined in a similar way as in the previous study of Konovalov et al. [30]. However, in the present work, a new model formulation was used. A very good agreement is obtained between the calculation and measurement in view of the shape of the flow curves and the absolute level of the calculated flow stress over the entire range of strain rates and temperatures.

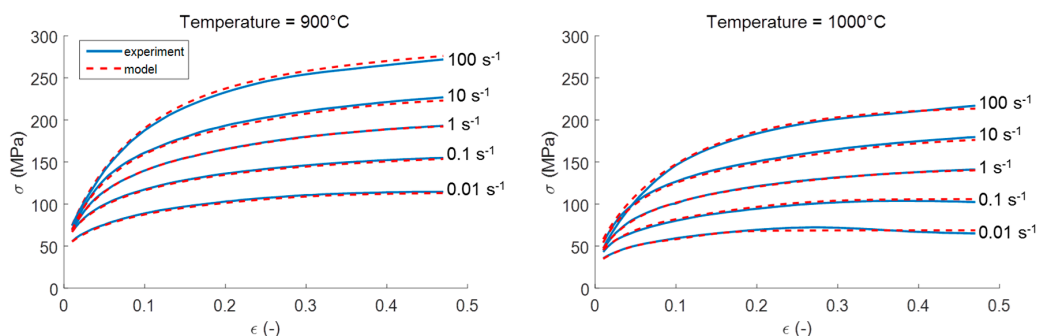


**Figure 10. Cont.**

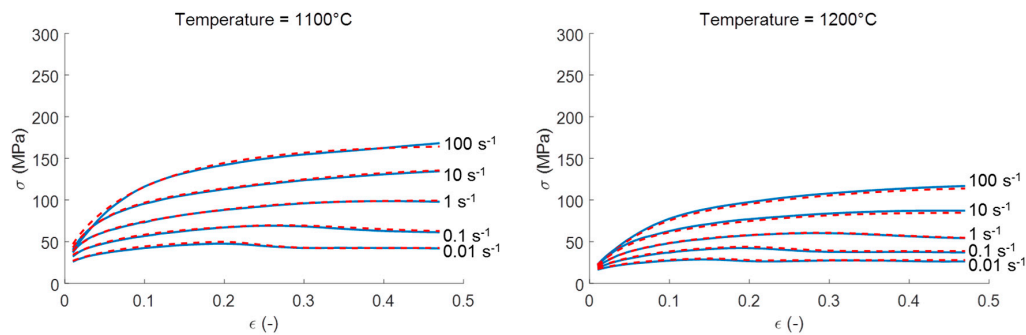


**Figure 10.** Model prediction vs. experimental data of 25MoCrS4 at various temperatures und strain rates.

The model shows a very high accuracy for a wide range of temperatures and strain rates. In Figure 11, the comparison between the calculated and measured flow stresses is shown for the TNB-V4-alloy for strain rates varying from  $0.001 \text{ s}^{-1}$  to  $0.5 \text{ s}^{-1}$  and for a temperature of  $1200^\circ\text{C}$  suitable for isothermal forging.

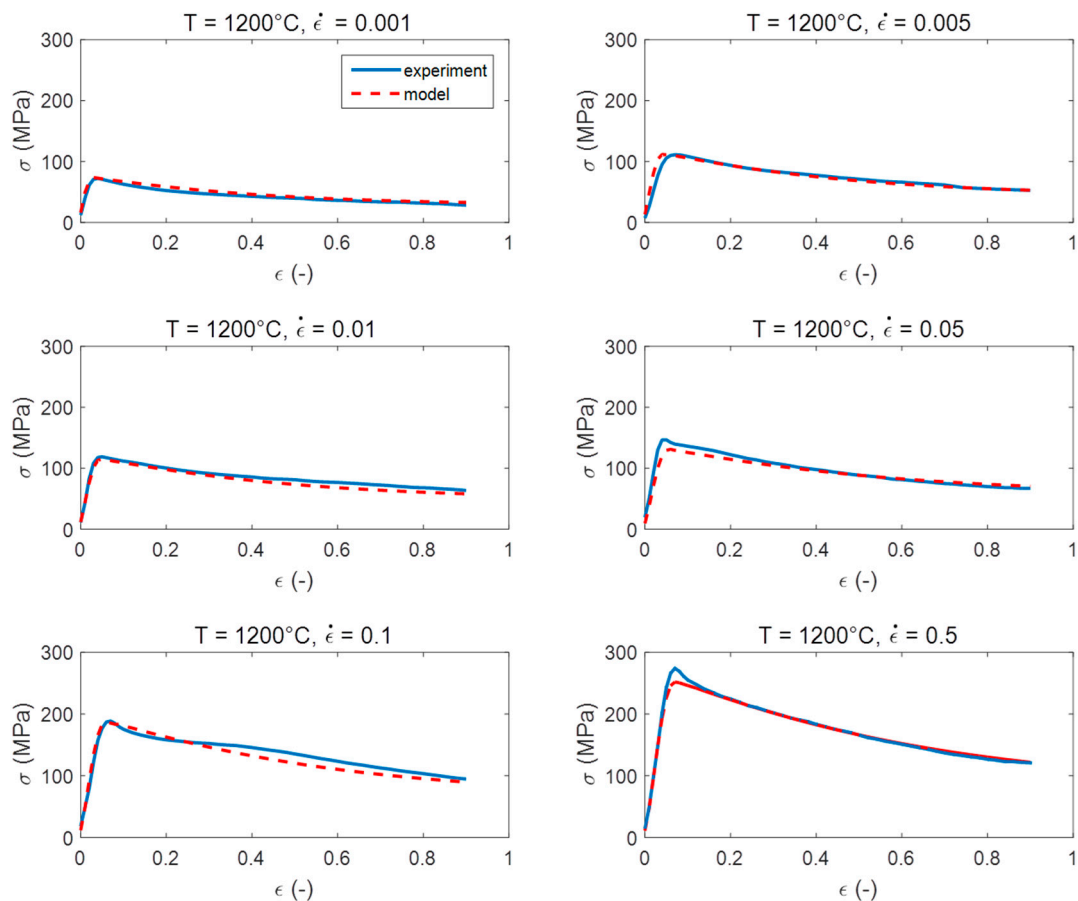


**Figure 11.** Model prediction vs. experimental data of TNB-V4-alloy at  $1200^\circ\text{C}$  and various strain rates.

The results indicate that the proposed strain hardening model can properly describe and predict the flow stress of the TiAl-alloy under isothermal forging conditions. The model accurately predicts the flow stress up to the peak stress and to some extent also the transition to the steady state.

The results show that for both 25MoCrS4 and TNB-V4, building a model from the behavior observed in Kocks-Mecking plots has the advantage that the model is consistent with the observed

strain hardening stages and shows a high accuracy. If only curve fitting in terms of stress strain curves is performed and valuable information provided by the Kocks-Mecking plots is neglected, inconsistencies and larger uncertainties of the model performance may be the consequence. For the 25MoCrS4, an intricate model was designed which takes the physics of dynamic recrystallization into account. For TNB-V4, both the strain hardening before the initiation of DRX and the softening kinetics are entirely phenomenological. For TiAl alloys in general, a deeper insight into the deformation mechanism leading to the observed behavior seems necessary. Reflecting the model behavior with the experimental results not only in stress-strain space but also in  $\theta$ - $\sigma$ -space, as proposed in this paper, yields important information to guide the model development.

## 6. Conclusions

In the present study the peculiarities of the work hardening and softening behavior of a Ti–44.5Al–6.25Nb–0.8Mo–0.1B (in at %) TNB-V4-alloy were investigated and compared to a typical case-hardening steel 25MoCrS4. The flow curves were analyzed using Kocks-Mecking plots in order to illustrate the difference in deformation behavior between a typical steel and the high Nb containing TiAl-alloy. Specific model equations for 25MoCrS4 and Ti–44.5Al–6.25Nb–0.8Mo–0.1B were derived based on the course of the Kocks-Mecking plots. The empirical equation proposed by Cingara and McQueen was used to model the work-hardening region for TNB-V4, since this model is able to show a concave down course in the Kocks-Mecking plot, as observed experimentally. A new model formulation capable of showing an inflection point was used for 25MoCrS4. For the DRX kinetics, a new formulation consistent with the Poliak-Jonas criterion was applied to 25MoCrS4. For TNB, a JMAK type kinetics was used, which describes all softening mechanisms without taking into account the physical background.

The following conclusions can be drawn from the presented studies:

- Kocks-Mecking plots reveal that in contrast to 25MoCrS4 steel the Ti–44.5Al–6.25Nb–0.8Mo–0.1B alloy neither shows a linear decrease of  $\theta$  (i.e., no stage-III hardening) nor does it exhibit a plateau (stage IV hardening) or an inflection point (marking the onset of DRX) at all forming conditions.
- The information obtained from Kocks-Mecking plots should be taken into account in the development of strain hardening models. Otherwise, inconsistencies, e.g., with the Poliak-Jonas criterion, may result.
- Both models show a high accuracy. They may hence be used in finite element simulations of metal forming processes. For TNB-V4, however, the complex microstructure evolution, i.e., the recrystallization of the individual phases, the reorientation of the lamellar colonies and flow localization effects during deformation need to be taken into account in continuative work.

**Acknowledgments:** The model development was performed as preliminary study in the project BA4253/2-1 funded by the German Research Foundation. M. Bambach and I. Sizova gratefully acknowledge the funding obtained.

**Author Contributions:** Bambach, M. devised the constitutive models, wrote and edited the manuscript; Sizova, I. analyzed the experimental data, performed the parameter identification and wrote parts of the manuscript; and Bolz, S. and Weiß, S. performed the microstructure analysis and interpretation of the obtained results and wrote the respective sections of the manuscript.

**Conflicts of Interest:** The authors declare no conflict of interest.

## References

1. Appel, F.; Wagner, R. Microstructure and deformation of two-phase  $\gamma$ -titanium aluminides. *Mater. Sci. Eng. Rep.* **1998**, *22*, 187–268. [[CrossRef](#)]
2. Dimiduk, D. Gamma titanium aluminide alloys—An assessment within the competition of aerospace structural materials. *Mater. Sci. Eng. A* **1999**, *263*, 281–288. [[CrossRef](#)]
3. Kabir, M.R.; Chernova, L.; Bartsch, M. Numerical investigation of room-temperature deformation behavior of a duplex type  $\gamma$ TiAl alloy using a multi-scale modeling approach. *Acta Mater.* **2010**, *58*, 5834–5847. [[CrossRef](#)]

4. Mecking, H.; Kocks, U.F. Kinetics of flow and strain-hardening. *Acta Metall.* **1981**, *29*, 1865–1875. [[CrossRef](#)]
5. Estrin, Y.; Mecking, H. A unified phenomenological description of work hardening and creep based on one-parameter models. *Acta Metall.* **1984**, *32*, 57–70. [[CrossRef](#)]
6. Bergström, Y. A dislocation model for the stress-strain behaviour of polycrystalline  $\alpha$ -Fe with special emphasis on the variation of the densities of mobile and immobile dislocations. *Mater. Sci. Eng.* **1970**, *5*, 193–200. [[CrossRef](#)]
7. Baragar, D.L. The high temperature and high strain-rate behaviour of a plain carbon and an HSLA steel. *J. Mech. Work. Technol.* **1987**, *14*, 295–307. [[CrossRef](#)]
8. Davenport, S.B.; Silk, N.J.; Sparks, C.N.; Sellars, C.M. Development of constitutive equations for modelling of hot rolling. *Mater. Sci. Technol.* **2013**, *16*, 539–546. [[CrossRef](#)]
9. Rao, K.P.; Hawbolt, E.B. Development of constitutive relationships using compression testing of a medium carbon steel. *J. Eng. Mater. Technol.* **1992**, *114*, 116. [[CrossRef](#)]
10. Cheng, L.; Xue, X.; Tang, B.; Kou, H.; Li, J. Flow characteristics and constitutive modeling for elevated temperature deformation of a high Nb containing TiAl alloy. *Intermetallics* **2014**, *49*, 23–28. [[CrossRef](#)]
11. Laasraoui, A.; Jonas, J.J. Prediction of steel flow stresses at high temperatures and strain rates. *Metall. Trans. A* **1991**, *22*, 1545–1558. [[CrossRef](#)]
12. Godor, F.; Werner, R.; Lindemann, J.; Clemens, H.; Mayer, S. Characterization of the high temperature deformation behavior of two intermetallic TiAl–Mo alloys. *Mater. Sci. Eng. A* **2015**, *648*, 208–216. [[CrossRef](#)]
13. Sellars, C.M.; McTegart, W.J. On the mechanism of hot deformation. *Acta Metall.* **1966**, *14*, 1136–1138. [[CrossRef](#)]
14. Hensel, M.; Spittel, T. *Ver- u. Entfestigung bei Warmumformung*; Dt. Verl. für Grundstoffindustrie: Leipzig, Germany, 1982.
15. He, X.; Yu, Z.; Liu, G.; Wang, W.; Lai, X. Mathematical modeling for high temperature flow behavior of as-cast Ti–45Al–8.5Nb–(W,B,Y) alloy. *Mater. Des.* **2009**, *30*, 166–169. [[CrossRef](#)]
16. Pu, Z.J.; Wu, K.H.; Shi, J.; Zou, D. Development of constitutive relationships for the hot deformation of boron microalloying TiAl–Cr–V alloys. *Mater. Sci. Eng. A* **1995**, *192–193*, 780–787. [[CrossRef](#)]
17. Deng, T.-Q.; Ye, L.; Sun, H.-F.; Hu, L.-X.; Yuan, S.-J. Development of flow stress model for hot deformation of Ti-47%Al alloy. *Trans. Nonferr. Met. Soc. China* **2011**, *21*, s308–s314. [[CrossRef](#)]
18. Nobuki, M.; Hashimoto, K.; Takahashi, J.; Tsujimoto, T. Deformation of cast TiAl intermetallic compound at elevated temperatures. *Mater. Trans. JIM* **1990**, *31*, 814–819. [[CrossRef](#)]
19. Fukutomi, H.; Nomoto, A.; Osuga, Y.; Ikeda, S.; Mecking, H. Analysis of dynamic recrystallization mechanism in  $\gamma$ -TiAl intermetallic compound based on texture measurement. *Intermetallics* **1996**, *4*, S49–S55. [[CrossRef](#)]
20. Kim, H.Y.; Sohn, W.H.; Hong, S.H. High temperature deformation of Ti–(46–48)Al–2W intermetallic compounds. *Mater. Sci. Eng. A* **1998**, *251*, 216–225. [[CrossRef](#)]
21. Fröbel, U.; Appel, F. Hot-workability of gamma-based TiAl Alloys during severe torsional deformation. *Metall. Mater. Trans. A* **2007**, *38*, 1817–1832. [[CrossRef](#)]
22. Kim, H.Y.; Hong, S.H. Effect of microstructure on the high-temperature deformation behavior of Ti–48Al–2W intermetallic compounds. *Mater. Sci. Eng. A* **1999**, *271*, 382–389. [[CrossRef](#)]
23. Semiatin, S.L.; Frey, N.; Thompson, C.R.; Bryant, J.D.; El-Soudani, S.; Tisler, R. Plastic flow behavior of Ti–48Al–2.5Nb–0.3Ta at hot-working temperatures. *Scr. Metall. Mater.* **1990**, *24*, 1403–1408. [[CrossRef](#)]
24. Wiezorek, J.M.K.; Deluca, P.M.; Mills, M.J.; Fraser, H.L. Deformation mechanisms in a binary Ti-48 at % Al alloy with lamellar microstructure. *Philos. Mag. Lett.* **1997**, *75*, 271–280. [[CrossRef](#)]
25. Schaden, T.; Fischer, F.D.; Clemens, H.; Appel, F.; Bartels, A. Numerical modelling of kinking in lamellar  $\gamma$ -TiAl based Alloys. *Adv. Eng. Mater.* **2006**, *8*, 1109–1113. [[CrossRef](#)]
26. McQueen, H.; Ryan, N. Constitutive analysis in hot working. *Mater. Sci. Eng. A* **2002**, *322*, 43–63. [[CrossRef](#)]
27. Kocks, U.F.; Mecking, H. A mechanism for static and dynamic recovery. In *Strength of Metals and Alloys*; Haasen, P., Gerold, V., Kostorz, G., Eds.; Pergamon Press: Oxford, UK, 1980; pp. 345–350.
28. Jonas, J.J.; Quennec, X.; Jiang, L.; Martin, É. The Avrami kinetics of dynamic recrystallization. *Acta Mater.* **2009**, *57*, 2748–2756. [[CrossRef](#)]
29. Bambach, M.; Sizova, I.; Bolz, S.; Weiß, S. Development of a dynamic recrystallization model for a  $\beta$ -solidifying titanium aluminide alloy using kocks-mecking plots. In Proceedings of the 19st ESAFORM Conference on Material Forming, Nantes, France, 27–29 April 2016.

30. Konovalov, S.; Henke, T.; Jansen, U.; Hardjosuwito, A.; Lohse, W.; Bambach, M.; Prahl, U. Test case gearing component. In *Integrative Computational Materials Engineering: Concepts and Applications of a Modular Simulation Platform*; Schmitz, G.J., Prahl, U., Eds.; John Wiley & Sons: Weinheim, Germany, 2012.
31. Semiatin, S.L.; Frey, N.; El-Soudani, S.M.; Bryant, J.D. Flow softening and microstructure evolution during hot working of wrought near-gamma titanium aluminides. *Metall. Mater. Trans. A* **1992**, *23*, 1719–1735. [[CrossRef](#)]
32. Lohmar, J.; Bambach, M. Influence of different interpolation techniques on the determination of the critical conditions for the onset of dynamic recrystallization. *Mater. Sci. Forum* **2013**, *762*, 331–336. [[CrossRef](#)]
33. Xiong, W.; Lohmar, J.; Bambach, M.; Hirt, G. A new method to determine isothermal flow curves for integrated process and microstructural simulation in metal forming. *Int. J. Mater. Form.* **2015**, *8*, 59–66. [[CrossRef](#)]
34. Bolz, S.; Oehring, M.; Lindemann, J.; Pyczak, F.; Paul, J.; Stark, A.; Lippmann, T.; Schrüfer, S.; Roth-Fagaraseanu, D.; Schreyer, A.; et al. Microstructure and mechanical properties of a forged  $\beta$ -solidifying  $\gamma$ -TiAl alloy in different heat treatment conditions. *Intermetallics* **2015**, *58*, 71–83. [[CrossRef](#)]
35. Fujiwara, T.; Nakamura, A.; Hosomi, M.; Nishitani, S.; Shirai, Y.; Yamaguchi, M. Deformation of polysynthetically twinned crystals of TiAl with a nearly stoichiometric composition. *Philos. Mag. A* **1990**, *61*, 591–606. [[CrossRef](#)]
36. Schwaighofer, E.; Clemens, H.; Lindemann, J.; Stark, A.; Mayer, S. Hot-working behavior of an advanced intermetallic multi-phase  $\gamma$ -TiAl based alloy. *Mater. Sci. Eng. A* **2014**, *614*, 297–310. [[CrossRef](#)]
37. Bariani, P.F.; Negro, T.D.; Bruschi, S. Testing and modelling of material response to deformation in bulk metal forming. *CIRP Ann. Manuf. Technol.* **2004**, *53*, 573–595. [[CrossRef](#)]
38. Bambach, M. Implications from Poliak—Jonas criterion for the construction of flow stress models incorporating dynamic recrystallization. *Acta Mater.* **2013**, *61*, 6222–6233. [[CrossRef](#)]
39. Luton, M.; Sellars, C. Dynamic recrystallization in nickel and nickel-iron alloys during high temperature deformation. *Acta Metall.* **1969**, *17*, 1033–1043. [[CrossRef](#)]
40. Beynon, J.H.; Sellars, C.M. Modelling microstructure and its effects during multipass hot rolling. *ISIJ Int.* **1992**, *32*, 359–367. [[CrossRef](#)]
41. Sellars, C.M. Modelling of structural evolution during hot working processes. In Proceedings of the International Symposium on Annealing Processes: Recovery, Recrystallisation and Grain Growth, Sheffield, UK, 8–12 September 1986; pp. 167–187.
42. Sandström, R.; Lagneborg, R. A model for hot working occurring by recrystallization. *Acta Metall.* **1975**, *23*, 387–398. [[CrossRef](#)]
43. Sommitsch, C.; Mitter, W. On modelling of dynamic recrystallisation of fcc materials with low stacking fault energy. *Acta Mater.* **2006**, *54*, 357–375. [[CrossRef](#)]
44. Cingara, A.; McQueen, H.J. New formula for calculating flow curves from high temperature constitutive data for 300 austenitic steels. *J. Mater. Process. Technol.* **1992**, *36*, 31–42. [[CrossRef](#)]



© 2016 by the authors; licensee MDPI, Basel, Switzerland. This article is an open access article distributed under the terms and conditions of the Creative Commons Attribution (CC-BY) license (<http://creativecommons.org/licenses/by/4.0/>).